Pulse stretch effects in the context of data-driven imaging methods

Jürgen Mann and German Höcht

Geophysical Institute, University of Karlsruhe, Germany

Summary

Conventional imaging methods cause an offset-dependent stretch of the seismic wavelet, even with a correct velocity model and kinematically exact stacking or migration operators. This stretch occurs either in the time domain during stacking or in the depth domain during pre-stack depth migration and deteriorates the resulting images.

In contrast, data-driven imaging methods like Multifocusing or Common-Reflection-Surface stack do not suffer from such pulse stretch phenomena. Thus, the image quality is improved and areas with high offset/traveltime ratio in the pre-stack data no longer have to be muted to the usual extent. We discuss the origin of the pulse stretch phenomenon and the behavior of the stacking parameters in data-driven imaging methods in order to avoid the stretch.

Introduction

Conventional imaging methods, irrespective if applied in the time or depth domain, systematically distort the wavelet with respect to its length and its shape, leading to a reduced frequency content and the risk of misinterpretation. These effects occur even if the stacking operators are kinematically correct as the finite length of the wavelet is not taken into account. This kind of unwanted changes of the wavelet do not occur during the Common-Reflection-Surface (CRS) stack and similar data-oriented imaging methods like Multifocusing (Berkovitch et al., 1994; Landa et al., 1999) or the delayed hyperbola approaches by de Bazelaire (1988); Thore et al. (1994). To explain this fact, we briefly review the reasons for the pulse stretch in conventional imaging methods for a simple example where the respective stacking operators are kinematically exact.

We discuss approximations for the stacking trajectories for neighboring samples along the wavelet in band-limited data and compare them to the stacking velocities determined by means of the CRS stack. It turns out that the optimum stacking velocity model is not smooth but reveals a systematic variation of the stacking velocity along the wavelet. Reformulated in terms of kinematic wavefield attributes, these variations vanish. Thus, these attributes provide a consistent parameterization of the reflection events and allow a more reliable extraction of information for subsequent processing steps like inversion (see also presentations P004, D27, and D31).

CMP traveltimes along the wavelet

Pulse stretch occurs either in the time domain due to the normal-moveout (NMO) correction or in the depth domain due to pre-stack migration (see, e. g., Tygel et al., 1994). Here, we restrict ourselves to the time domain and idealized situations with kinematically exact stacking operators to focus on the pulse stretch effect. For the sake of simplicity, we consider the simplest situation, a plane horizontal reflector with homogeneous overburden. For a reflector at depth z_0 and a velocity v_0, the kinematic reflection response is given by

$$t(h) = \frac{2}{v_0}\sqrt{h^2+z_0^2} = \sqrt{t_0^2+\frac{4h^2}{v_0^2}}, \qquad (1)$$

where $t_0 = 2z_0/v_0$ denotes the zero-offset (ZO) traveltime and h is the half-offset. For a medium without attenuation, the pre-stack data can be represented as a convolution of the wavelet and the kinematic reflection response (phase shifts are not considered here): the pulse length is identical for all shot and receiver locations. An undistorted result can be obtained by stacking along the kinematic reflection response (1) vertically shifted by Δt to all locations within the wavelet of length T:

$$\tilde{t}(h,\Delta t) = \sqrt{t_0^2+\frac{4h^2}{v_0^2}}+\Delta t \quad \text{with} \quad -\frac{T}{2} \le \Delta t \le \frac{T}{2}, \qquad (2)$$

where we assume that the wavelet is centered around the traveltime t. An NMO correction applied with the velocity v_0 yields the correct traveltimes for the center of the wavelet. However, the NMO operator attached to a neighboring ZO traveltime differs from the corresponding iso-phase curve (2). The time shift between two NMO operators with the same stacking velocity but attached to different ZO traveltimes is not constant but decreases with increasing offset. This leads to the well-known pulse stretch effect.

Alternative approximation of the stacking velocity

A (locally) constant stacking velocity model is not suited to describe the iso-phase curves in the input data as it leads to pulse stretch. Thus, a more appropriate description of the stacking velocity along the seismic wavelet is required. Expressing the shifted hyperbola (2) in terms of the ZO traveltime t_0 and the velocity v_0 defined at the center of the wavelet, we obtain a new stacking velocity at $t_0+\Delta t$:

$$\tilde{v}^2(\Delta t,h) = \frac{2h^2 v_0^2}{2h^2+v_0^2\Delta t\, t(h) - v_0^2 t_0 \Delta t}. \qquad (3)$$

Due to its offset-dependency, the shifted hyperbola (2) cannot be parameterized by means of a single stacking velocity: an exact description of the iso-phase curves in the data would require an additional parameter, e. g., the time shift Δt itself. To avoid this, a reasonable approximation of $\tilde{v}$ is required. Usually, $\tilde{v}$ is assumed to coincide with v_0, which only holds for large offset.

For the simulation of ZO sections, a more reasonable approach is to require a constant curvature at offset zero of all stacking hyperbolae such that the time shift between neighboring operators is almost constant for small offsets. This leads to the approximate stacking velocity

$$\tilde{v}_c^2(\Delta t) \approx \frac{t_0}{t_0+\Delta t}v_0^2. \qquad (4)$$

The operators defined by v_0 and $\tilde{v}_c$ are shown in Figure 1 together with the exact iso-phase curves. In addition, the operators for a local stacking velocity gradient are displayed.

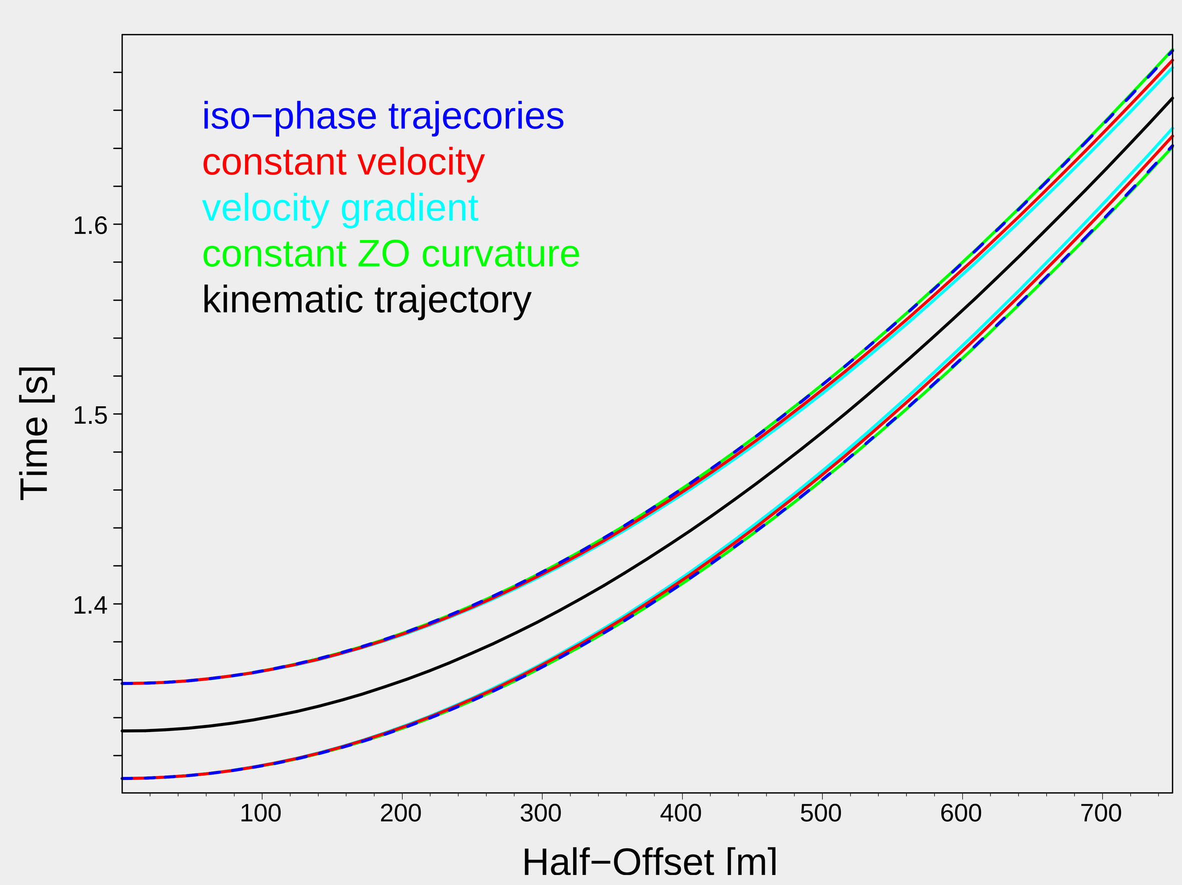

Figure 1: Stacking operators for a horizontal reflector at 1000 m depth, $v_0 = 1500$ m/s, and a pulse length of 50 ms. The considered local velocity gradient is 400 m/s[2]. The constant ZO curvature trajectories (green) almost coincide with the iso-phase trajectories (blue).

If we calculate the pulse stretch occurring for the different stacking velocities (Figure 2), the constant ZO curvature causes by far the smallest distortion of the wavelet. Actually, the wavelet is even slightly compressed for large offsets. A usually present velocity gradient in the stacking velocity model leads to an even larger stretch than a constant velocity.

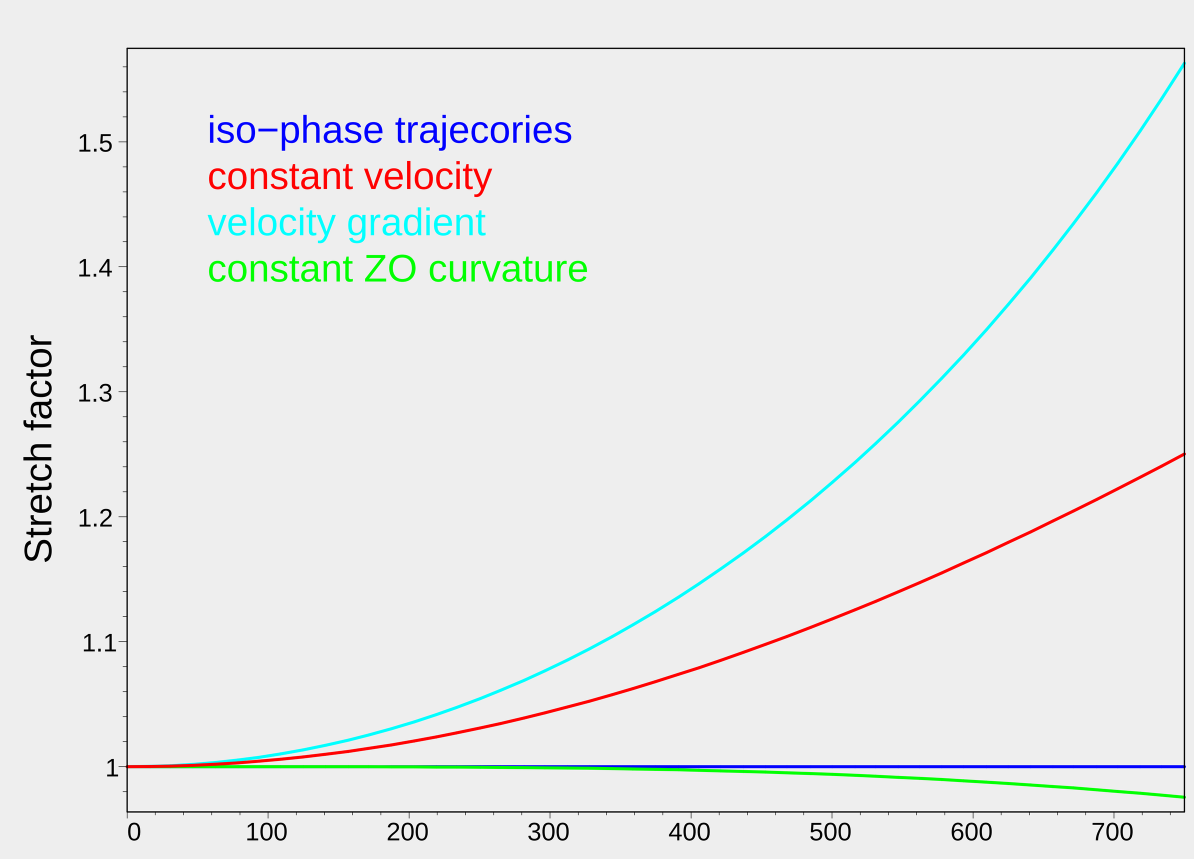

Figure 2: Pulse stretch functions associated with the traveltime curves in Figure 1, i. e., wavelet length over traveltime difference.

Numerical example for a 1-D model

To analyze the behavior of the stacking velocity derived by means of the CRS stack method, we used the same 1-D model as before, but now with three reflectors at depths $z_i = 1000, 1080, 1160$ m consisting of pure density contrasts, only. A CMP gather with half-offsets up to 500 m was simulated with a fold of 31 and a zero-phase Ricker wavelet with 30 Hz peak frequency. The forward-modeled ZO trace is shown in Figure 3a.

In the scope of this presentation, we cannot discuss the CRS stack method in detail, more information can be found in the related presentations (see below). The basic features of the CRS stack for 2-D ZO simulation are as follows:

- the CRS stack can be seen as a generalized velocity analysis and stacking tool
- for the considered case, three stacking parameters or *kinematic wavefield attributes* are used
- the generalized velocity analysis is performed *automatically* at *every ZO location* to be simulated
- a *spatial* stacking aperture is used, thus leading to higher stability and signal-to-noise ratio compared to conventional methods

With an appropriate coherence criterion like semblance, the CRS operator is fit to iso-phase surfaces of the reflection events. Consequently, there is no reason for pulse stretch. The first step of the CRS stack implementation is confined to the CMP gathers of the data, i. e., an *automatic* CMP stack according to Equation (1). This first initial processing step is sufficient to relate the advantageous approximation of the stacking velocity $\tilde{v}_c$ to the data-driven imaging approach.

The result of the automatic CMP stack is shown on the right hand side of Figure 3a. The original wavelet is recovered almost exactly. The coherence along the stacking operator (Figure 3b) shows where the events have been located and the wavefield attributes are reliable. At locations with low coherence, the attributes are meaningless as there is nothing coherent to be stacked at all.

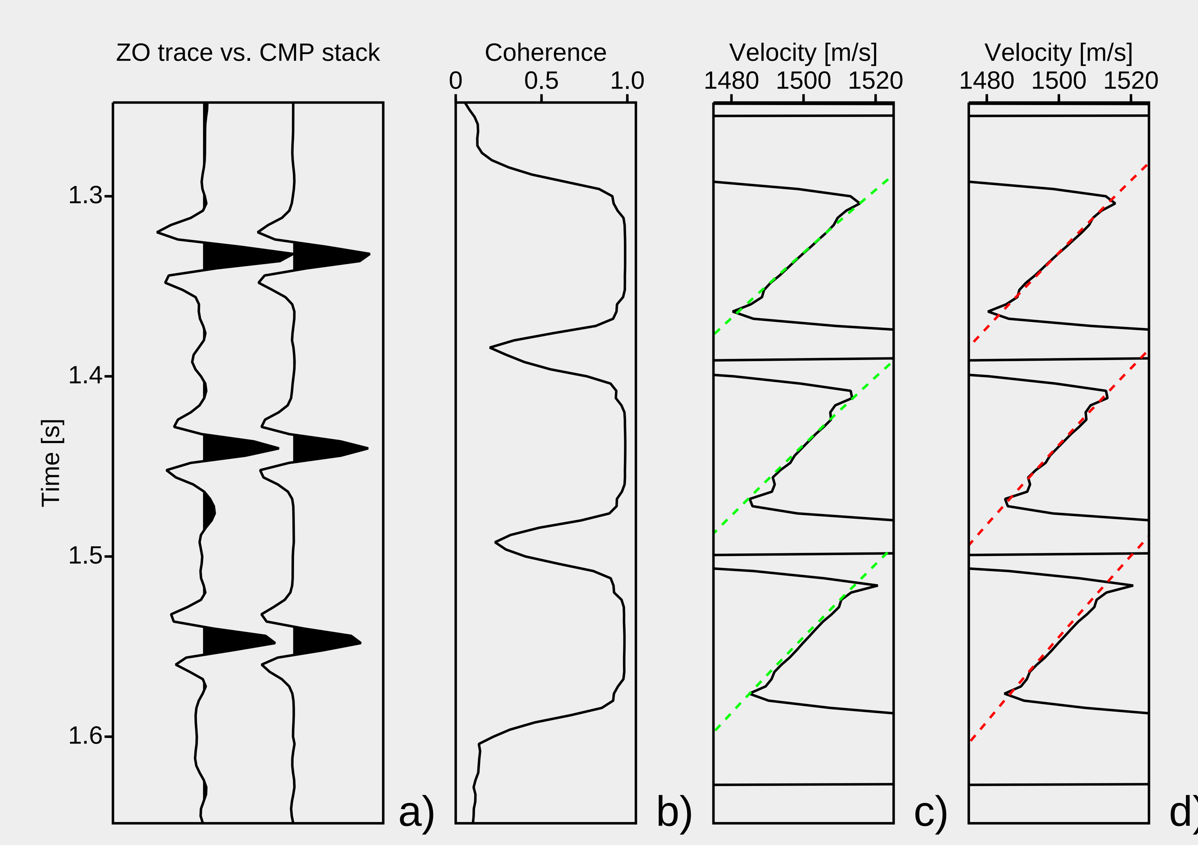

Figure 3: a) modeled ZO trace (left) versus simulated ZO trace obtained (right) obtained from the automatic CMP stack. b) coherence along the stacking operator. Determined stacking velocity (black) versus c) stacking velocity for constant ZO curvature, i. e., $\tilde{v}_c$ (green), d) stacking velocity providing the best possible kinematic fit to the iso-phase trajectories (red).

The stacking velocity determined by the automatic CMP stack is depicted as black line in Figure 3c and Figure 3d. It exposes a characteristic "jig saw" appearance as it *decreases* along the wavelet with *increasing* traveltime. This significantly deviates from the usually applied smooth stacking velocity sections.

Let us now compare this behavior with the approximate stacking velocity $\tilde{v}_c$, shown as green line in Figure 3c. This approximation is very close to the data-derived stacking velocity. However, the constant ZO curvature approximation refers to offset zero, whereas the CRS stack is applied in a finite aperture around ZO. Thus, one should expect that the velocity analysis yields a stacking velocity which provides, in a least squares sense, the best possible fit to the iso-phase trajectory within the aperture. We calculated this optimum stacking velocity by minimizing the squared deviation from the actual traveltimes. Shown as red line in Figure 3d, this optimum stacking velocity hardly deviates from the constant ZO curvature approximation. Thus, the latter represents a suitable approximation, far more accurate than a smooth stacking velocity model.

Pulse stretch effects in the context of data-driven imaging methods

Jürgen Mann and German Höcht
Geophysical Institute, University of Karlsruhe, Germany

Moveout-corrected CMP gathers

Below, the moveout-corrected CMP gathers are shown for the different functions of the stacking velocity. To emphasize the details, only the first reflection event is displayed. Obviously, the usual situation, increasing stacking velocity with increasing time (Figure 4), leads to the largest pulse stretch and would already require muting to preserve the wavelet. In case of a constant stacking velocity (Figure 5), the pulse stretch is less severe. However, it will still be significant for large offset to traveltime ratios. In contrast, the NMO correction with the stacking velocity approximation $\tilde{v}_c$ for constant ZO curvature (Figure 6) preserves the wavelet almost perfectly. The small expected compression of the wavelet can hardly be observed. The result for the velocity providing the best kinematic fit (corresponding to the red line in Figure 3d) looks just the same and is, thus, not displayed. Finally, the NMO correction was performed with the stacking velocities determined by the CRS stack (Figure 7). As expected, no pulse stretch can be observed and the result almost coincides with Figure 6.

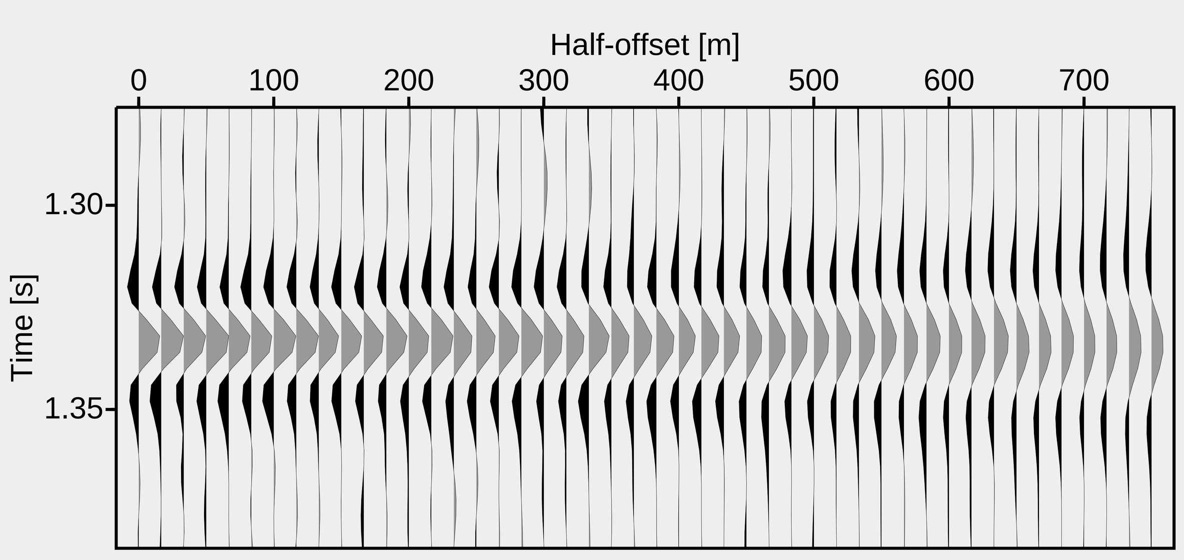

NMO correction with velocity gradient

Figure 4: CMP gather after NMO correction with a (local) velocity gradient of 400 m/s^2 and $v = 1500$ m/s at 1.33 s.

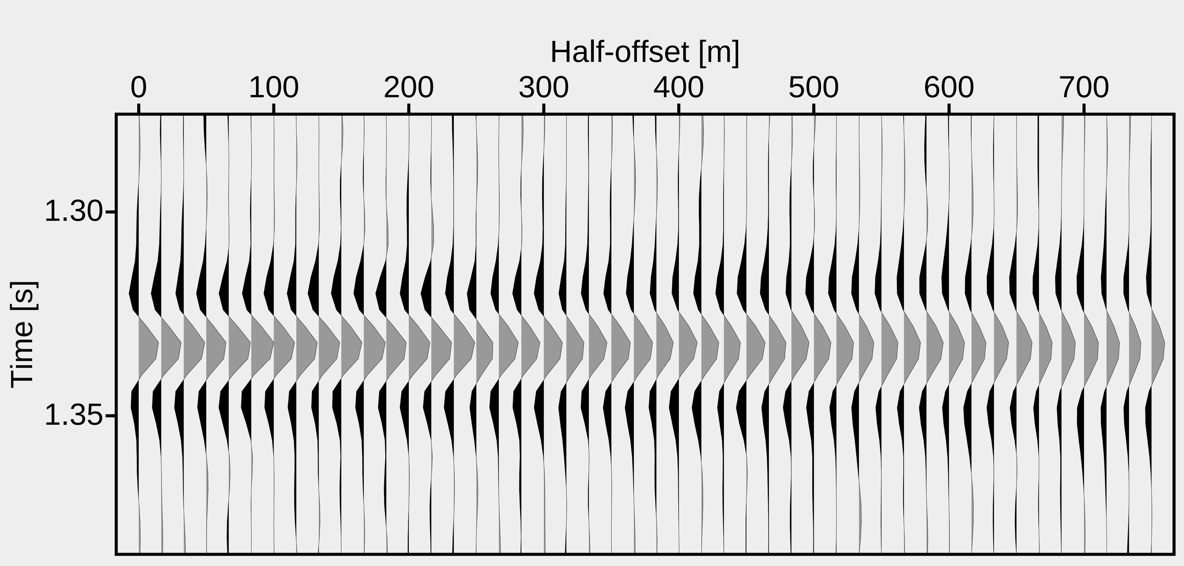

NMO correction with constant velocity

Figure 5: CMP gather after NMO correction with constant velocity 1500 m/s.

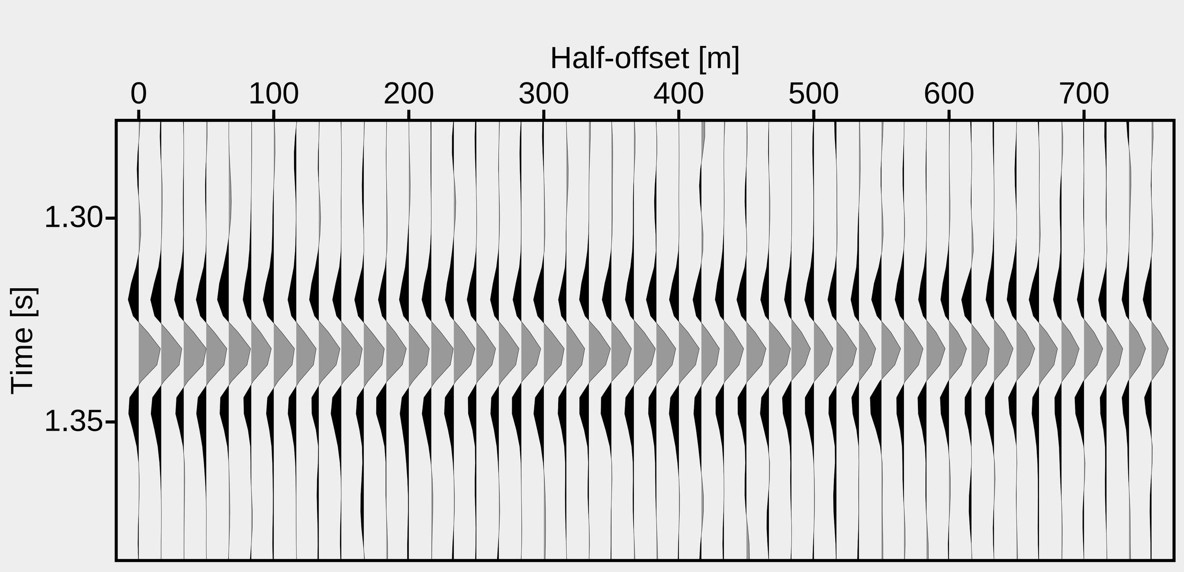

NMO correction with constant ZO curvature

Figure 6: CMP gather after NMO correction with velocity for constant ZO curvature according to Equation (4).

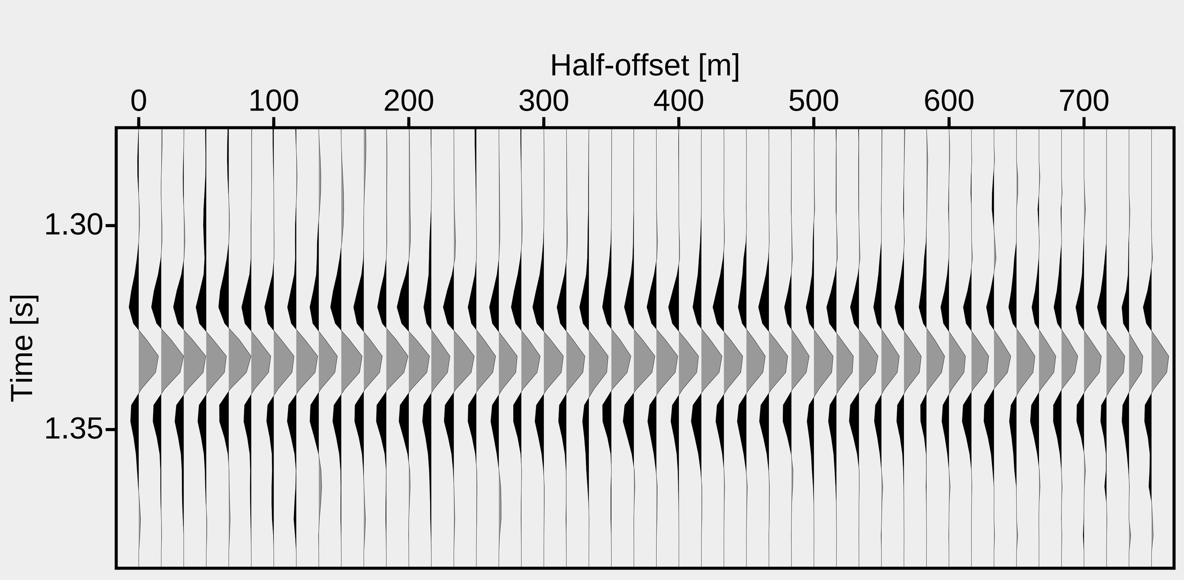

NMO correction with CRS attributes

Figure 7: CMP gather after NMO correction with stacking velocity from the automatic CMP stack.

Behavior of the kinematic wavefield attributes

In the following, we will reformulate the preceeding sections in terms of the kinematic wavefield attributes of the CRS stack approach. Expressed in terms of midpoint coordinate x_m and half-offset h, the second-order traveltime approximation reads

$$t^2_{\text{hyp}}(x_m, h) = \left[t_0 + \frac{2\sin\alpha\,(x_m - x_0)}{v_0}\right]^2 + \frac{2\,t_0\cos^2\alpha}{v_0}\left[\frac{(x_m - x_0)^2}{R_N} + \frac{h^2}{R_{\text{NIP}}}\right], \tag{5}$$

where v_0 represents the near-surface velocity and (t_0, x_0) is the considered ZO location. The CRS operator is parameterized by three kinematic wavefield attributes defined at the surface location x_0, namely α, the emergence angle of the ray normal to the reflector, R_{NIP}, the radius of the normal-incidence-point (NIP) wavefront, and R_N, the radius of the normal wavefront. These attributes are related to the local properties of a reflector segment in depth, namely its location, dip, and curvature, by means of two so-called eigenwave experiments (see, e. g., Jäger et al., 2001): in a first experiment, a point source is placed at the NIP and leads to the NIP wavefront that emerges at x_0 with the radius of curvature R_{NIP}. The second experiment is an exploding reflector experiment, the corresponding normal wavefront emerges with a radius of curvature R_N. The common propagation direction of both wavefronts is given by α.
For the simple 1-D model considered above, all rays are vertical and all normal wavefronts are plane, i. e., $\alpha = 0$ and $R_N = \pm\infty$ for all three events. Accordingly, the CRS operator reduces to

$$t_{\text{1-D}}(h) = \sqrt{t_0^2 + \frac{2\,t_0\,h^2}{v_0\,R_{\text{NIP}}}} \tag{6}$$

for any midpoint location x_m. For the center of the wavelet, this represents the exact kinematic reflection responses of the three reflectors with $R_{\text{NIP}} = z_i$, respectively. This is an alternative formulation of the CMP moveout formula (1). Reformulating Equation (4) in terms of R_{NIP} we readily observe that R_{NIP} remains constant along the wavelet, i. e., $R_{\text{NIP}}(t_0) = \tilde{R}_{\text{NIP}}(t_0 + \Delta t)\ \forall \Delta t$. Obviously, this is equivalent to the assumption of constant ZO curvature. Indeed, the NIP wavefront radius obtained by means of the CRS stack (Figure 8) is almost constant for each event. Thus, this radius appears to be a more natural parameter for the traveltime curves.

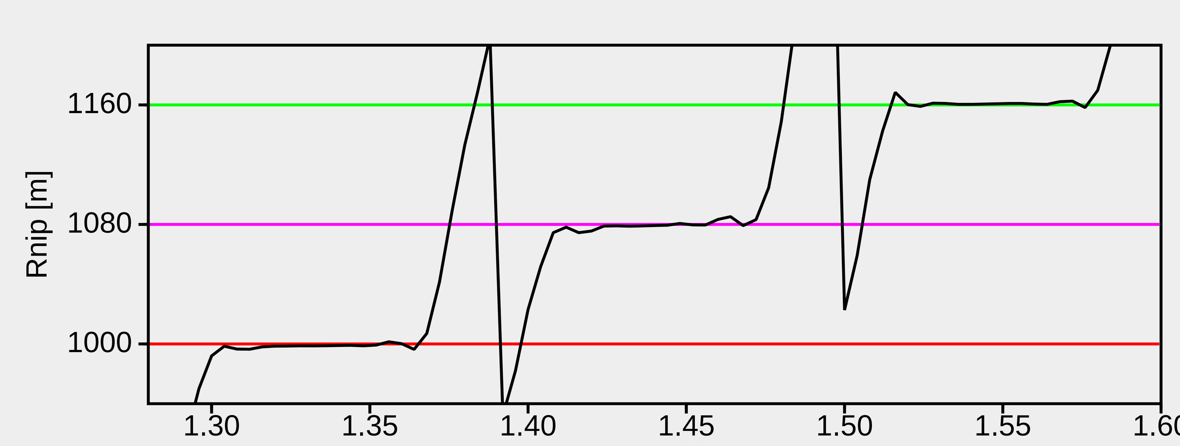

Figure 8: Radius of the NIP wavefront obtained with the automatic CMP stack. R_{NIP} is virtually constant along the wavelet and, for this simple model, coincides with the reflector depths $z_i = 1000$, 1080, and 1160 m (colored lines).

So far, we only considered a 1-D model and the CMP configuration. Let us now use the entire spatial CRS operator and an arbitrary 2-D model. As the emergence angle α is dominated by the linear term in Equation (5), α is not expected to vary along the wavelet. This behavior can be observed in the CRS stack results, too. Thus, $\cos^2\alpha$ only appears as a constant factor in the last term of Equation (5), such that the considerations for the 1-D model also hold for a 2-D model in the CMP configuration.
For other configurations where $x_m \neq x_0$, the linear term does not cause any pulse stretch as α is constant. Only the quadratic terms have to be considered. Again, as the CRS stacking operator is fit to iso-phase surfaces in the pre-stack data, no pulse stretch will occur. However, the radius of curvature R_N of the normal wave will not remain exactly constant along the wavelet: the quadratic term proportional to $\sin^2\alpha$ leads to some variations of R_N in case of large emergence angles. In practice, this is no significant problem: firstly, the applied stacking aperture along the midpoint axis is usually smaller than along the offset axis. Secondly, the curvature of reflection events in the ZO section is usually smaller than in the CMP gather. Thus, the influence of the quadratic terms is strongest in the CMP gather.

Conclusions

We briefly reviewed the origin of the offset-dependent pulse stretch in conventional time domain processing with constant or smooth stacking velocity models. A stretch-free imaging with optimally recovered wavelet is not possible with such models, as the band-limited nature of data is ignored.
We discussed an approximation of the stacking velocity variation along the wavelet that is well suited for the simulation of undistorted ZO sections. In contrast to the usually applied smooth stacking velocity models, the approach predicts a systematic velocity decrease with increasing traveltime along the wavelet of each reflection event. Thus, the limited bandwidth of the data is explicitely taken into account and wavelet distortions due to pulse stretch are avoided.
A comparison with CRS stack results for a 1-D model demonstrated that data-driven imaging methods automatically avoid the pulse stretch and introduce a systematic variation of the stacking velocity very similar to the predicted behavior. In other words, data-driven imaging methods performing generalized velocity analysis at *every* ZO location to be simulated implicitly consider the band-limited nature of seismic reflection data. Subsequent processes directly benefit from the input without pulse stretch.
Reformulated in terms of the kinematic CRS wavefield attributes, the variation of the stacking parameters along the wavelet vanishes. Thus, the radii of wavefront curvatures involved in the CRS stack approach provide a more appropriate parameterization of the reflection events. This is an important fact for applications that are based on picked traveltimes and CRS attributes, e. g., inversion (generalized Dix-type or tomographic, see related presentations below): samples picked out of phase do not lead to wrong attributes.

References

Berkovitch, A., Gelchinsky, B., and Keydar, S. (1994). Basic formulae for multifocusing stack. 56th Mtg. Eur. Assoc. Expl. Geophys., Extended Abstracts. Session: P140.

de Bazelaire, E. (1988). Normal moveout revisited – inhomogeneous media and curved interfaces. *Geophysics*, 53(2):143–157.

Jäger, R., Mann, J., Höcht, G., and Hubral, P. (2001). Common-reflection-surface stack: Image and attributes. *Geophysics*, 66(1):97–109.

Landa, E., Gurevich, B., Keydar, S., and Trachtman, P. (1999). Application of multifocusing method for subsurface imaging. *J. Appl. Geoph.*, 42(3,4):283–300.

Mann, J. (2002). *Extensions and applications of the Common-Reflection-Surface Stack method*. Logos Verlag, Berlin.

Mann, J., Jäger, R., Müller, T., Höcht, G., and Hubral, P. (1999). Common-reflection-surface stack – a real data example. *J. Appl. Geoph.*, 42(3,4):301–318.

Thore, P. D., de Bazelaire, E., and Ray, M. P. (1994). Three-parameter equation: An efficient tool to enhance the stack. *Geophysics*, 59(2):297–308.

Tygel, M., Schleicher, J., and Hubral, P. (1994). Pulse distortion in depth migration. *Geophysics*, 59(10):1561–1569.

Acknowledgments

This work was kindly supported by the sponsors of the *Wave Inversion Technology (WIT) Consortium*, Karlsruhe, Germany.

Related presentations

P004 An integrated data-driven approach to seismic reflection imaging, *Hertweck et al.*

D17 CRS imaging of 3-D seismic data from the active continental margin offshore Costa Rica, *Trappe et al.*

D18 Residual static correction by means of kinematic wavefield attributes, *Koglin and Ewig*

D27 Determination of velocity models from data-derived wavefront attributes, *Duveneck*

D31 3-D macro-velocity inversion by means of kinematic wavefield attributes, *Höcht et al.*